DRAFT VERSION JULY 19, 2016
Preprint typeset using LaTeX style emulateapj v. 01/23/15

arXiv:1607.04674v1 [astro-ph.CO] 15 Jul 2016

# MERGER HYDRODYNAMICS OF THE LUMINOUS CLUSTER RXJ1347.5-1145

C.D. KREISCH[1,2], M.E. MACHACEK[3], C. JONES[3], S.W. RANDALL[3]
[1] Max Planck Institute for Astrophysics
Karl-Schwarzschild-Straße 1, 85748 Garching bei München, Germany
[2] Department of Physics, Washington University in St. Louis
One Brookings Drive, St. Louis, MO 63130 and
[3] Harvard-Smithsonian Center for Astrophysics
60 Garden Street, Cambridge, MA 02138 USA
*Draft version July 19, 2016*

## ABSTRACT

We present an analysis of the complex gas hydrodynamics in the X-ray luminous galaxy cluster RXJ1347.5-1145 caught in the act of merging with a subcluster to its southeast using a combined 186 ks *Chandra* exposure, 2.5 times greater than previous analyses. The primary cluster hosts a sloshing cold front spiral traced by four surface brightness edges $5\farcs85^{+0.04}_{-0.03}$ west, $7\farcs10^{+0.07}_{-0.03}$ southeast, $11\farcs5^{+1.3}_{-1.2}$ east, and $16\farcs7^{+0.3}_{-0.5}$ northeast from the primary central dominant galaxy, suggesting the merger is in the plane of the sky. We measure temperature and density ratios across these edges, confirming they are sloshing cold fronts. We observe the eastern edge of the subcluster infall shock, confirming the observed subcluster is traveling from the southwest to the northeast in a clockwise orbit. We measure a shock density contrast of $1.38^{+0.16}_{-0.15}$ and infer a Mach number $1.25 \pm 0.08$ and a shock velocity of $2810^{+210}_{-240}$ km s$^{-1}$ . Temperature and entropy maps show cool, low entropy gas trailing the subcluster in a southwestern tail, consistent with core shredding. Simulations suggest a perturber in the plane of the sky on a clockwise orbit would produce a sloshing spiral winding counterclockwise, opposite to that observed. The most compelling solution to this discrepancy is that the observed southeastern subcluster is on its first passage, shock heating gas during its clockwise infall, while the main cluster's clockwise cold front spiral formed from earlier encounters with a second perturber orbiting counterclockwise.

*Subject headings:* galaxies: clusters: general – galaxies: interactions – X-rays: galaxies: clusters – galaxies: clusters: individual (RXJ1347.5−1145)

## 1. INTRODUCTION

The growth of structure across cosmic time provides an important probe of cosmology. The evolution of the galaxy cluster mass function with redshift places significant constraints on the dark energy equation of state, with the greatest sensitivity found at the high mass end (Vikhlinin et al. 2009a,b). Since the baryon distribution in massive galaxy clusters is dominated by hot, X-ray emitting gas tracing the cluster dark matter potential, X-ray observations provide a natural tool to identify clusters. If the cluster is relaxed and the gas in hydrostatic equilibrium, these observational measures allow us to calculate the cluster mass. However, in the current hierarchical model for structure formation, massive clusters grow through mergers between galaxy groups and less massive clusters, that formed along overdense filaments in the cosmic web. Thus mergers are expected to be common. Kinetic energy from the merging partner is converted mainly to thermal energy in the form of shocks and turbulence in the cluster gas, profoundly affecting the evolution of the ICM (Fujita et al. 2004a,b,c; ZuHone et al. 2010, 2011). Non-hydostatic gas motions induced by the merger ('sloshing') are long lasting on timescales of order gigayears. Their characteristic signatures in X-ray observations, i.e. multiple surface brightness discontinuities (cold fronts) and/or sweeping spiral features in temperature and surface brightness, have been noted in many galaxy groups and clusters (e.g. see review by Markevitch & Vikhlinin 2007; Ascasibar & Markevitch 2006; Paterno-Mahler et al. 2013; Randall et al. 2009; Machacek et al. 2011).

The study of these merger-induced gas motions and entropy exchanges in massive clusters are key to understanding (1) the properties and evolution of the ICM and (2) how the departures from hydrostatic equilibrium affect uncertainties in the cluster mass determinations used to constrain cosmology.

Outstanding questions include:

- What role do merger shocks play in heating the cluster gas (ZuHone et al. 2010)?
- Does sloshing inhibit or promote cooling in the cluster core (ZuHone et al. 2010, 2011)?
- What can the morphology of the cold fronts and spirals tell us about the merger history of the cluster, cluster magnetic fields, or microphysics of the gas (see, e.g. review by Markevitch & Vikhlinin 2007; Roediger et al. 2012b; Roediger & Zuhone 2012; Roediger et al. 2012a, 2013a,b)?
- Does gas sloshing amplify magnetic fields and reaccelerate electrons, creating radio mini-halos found to be correlated with cold front edges in some clusters (Gitti et al. 2002; Gitti & Schindler 2004; Mazzotta & Giacintucci 2008; ZuHone et al. 2013)?

Progress on these questions will be found by a comparison of deep X-ray observations of relatively nearby ($z \lesssim 0.5$), massive, merging galaxy clusters, where gas temperatures and densities at cold fronts, shocks, and sloshing spirals can be well studied, with high resolution numerical simulations that connect the observed X-ray features with the orbital history of the merger and the microphysical properties of the surrounding gas.

ckreisch@wustl.edu

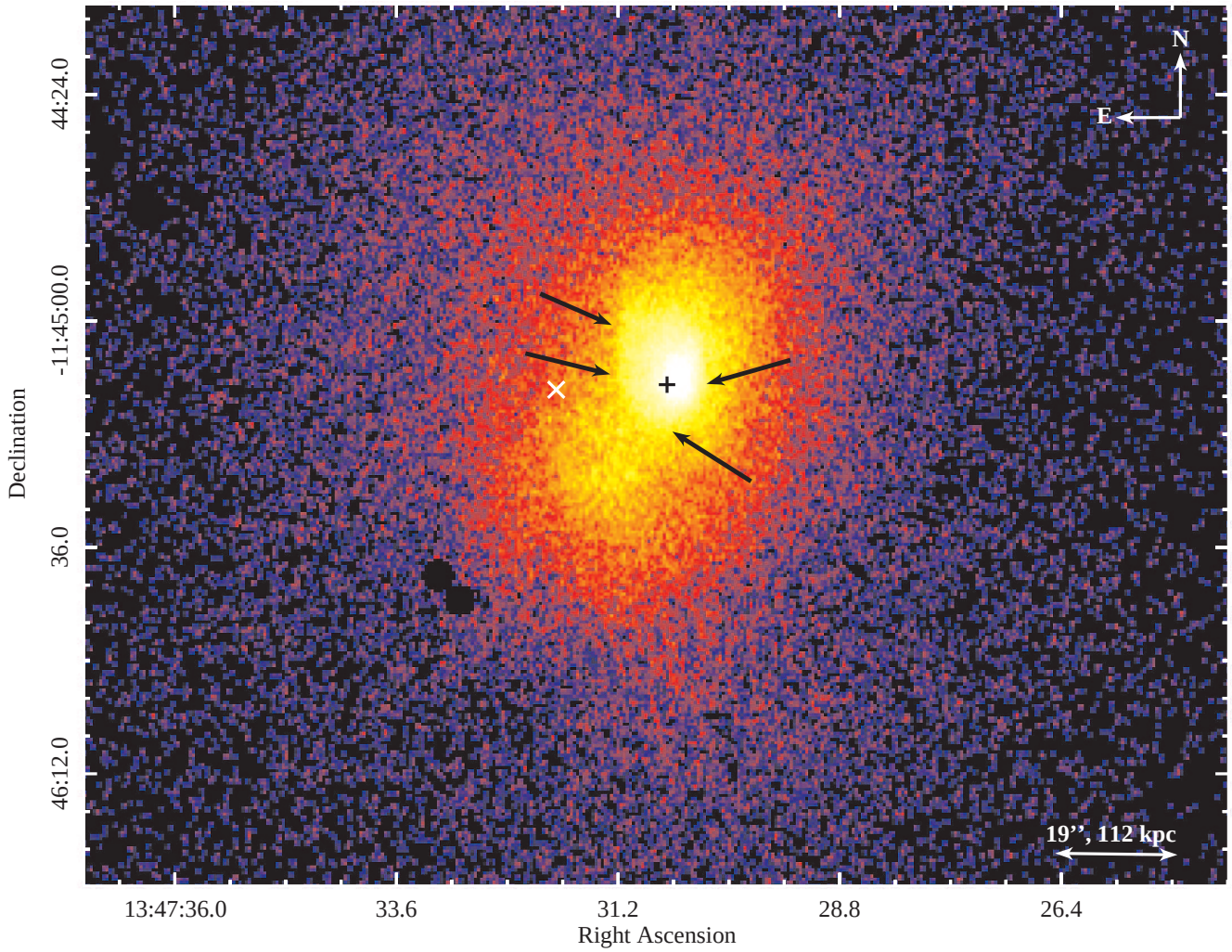


FIG. 1.— Chandra background subtracted, exposure corrected, combined 0.5-2.5 keV full resolution (1 pixel = $0.''492 \times 0.''492$) image of RXJ1347 with log scale. The primary cD galaxy is labeled with a black cross and the subcluster cD galaxy is labeled with a white x. Arrows point to edges forming a spiral pattern.

In this paper we use new and archival X-ray observations and archival Sunyaev-Zel'dovich effect (SZE) observations from the literature to characterize the cold fronts, shocks, and sloshing in RXJ1347.5−1145 (RXJ1347). With a 2−10 keV X-ray luminosity of $6 \times 10^{45}$ erg s$^{-1}$, RXJ1347 is the most X-ray luminous galaxy cluster found in the Rosat All Sky Survey (Schindler et al. 1995) and is still one of the more X-ray luminous galaxy clusters known. RXJ1347 is a massive, highly evolved cool core cluster, yet still actively merging with a less massive subcluster. Cool core clusters often show signatures of gas sloshing due to the presence of easily disturbed low entropy gas in their cores (Markevitch & Vikhlinin 2007). This makes RXJ1347 an ideal laboratory to study the on-going evolution of the bright end of the cluster luminosity function. It has been widely studied across many wavebands (see, e.g. Johnson et al. 2012, for a review). Optical spectroscopic surveys of its galaxy population yield a velocity dispersion and dynamical mass within $r_{200}$ for RXJ1347 of $\sigma = 1163 \pm 97$ km s$^{-1}$ and $1.16^{+0.32}_{-0.27} \times 10^{15} M_{\odot}$, respectively (Lu et al. 2010; Cohen & Kneib 2002). Lu et al. (2010) also found that RXJ1347 resides on a large scale filament, separated from a less massive galaxy cluster (RXJ1347-SW) by $\sim 7$ Mpc in projection and 4000 km s$^{-1}$ in radial velocity and with an excess of galaxies in between. Although the large velocity difference between the two clusters makes it unlikely that they are interacting, continued merging activity of RXJ1347 with other subclusters embedded within the same large scale filament would be expected in hierarchical cosmological models. The cluster K-band light is dominated by the two brightest cluster galaxies (BCGs). One, at (RA $13^h47^m30.7^s$, Dec $-11°45'10.''1$ ) near the peak of the X-ray surface brightness, is assumed to be the central dominant galaxy of the primary cluster, and the second, at (RA $13^h47^m31.9^s$, Dec $-11°45'10.''9$) lies $18''$ to the east. Given the second galaxy's relative radial velocity difference of only $\sim 100$ km s$^{-1}$ with respect to the primary cluster BCG, it has been interpreted as the central dominant galaxy of a merging subcluster. Surface mass density maps from weak and strong lensing show a general elongation in the mass concentration in the direction of the second BCG. However, they do not show a clear mass concentration peak there (Bradač et al. 2008; Köhlinger & Schmidt 2014).

Early X-ray observations by *Chandra* (Allen et al. 2002) and *XMM-Newton* (Gitti & Schindler 2004) found excess X-ray emission $\sim 20''$ southeast of the primary BCG, which we now interpret as emission from hot gas in a merging subcluster. Deeper *Chandra* observations have revealed two sloshing cold fronts in the primary cluster as a result of a recent merger (Johnson et al. 2012).

Sunyaev-Zel'dovich observations have played a critical role in understanding the merging subcluster's gas dynamics. Observations by Komatsu et al. (2001) with the Nobeyama 45 m telescope at 150 GHz first showed a significant SZ decrement $\sim 20''$ southeast of the primary cluster, suggesting RXJ1347 is a disturbed system that has recently undergone a merger (Kitayama et al. 2004). Higher resolution observations with the MUSTANG camera on the Green Bank Telescope at 90 GHz indicated the SZ decrement likely corresponds to shock heated gas from the merging subcluster (Mason et al. 2010; Korngut et al. 2011). A higher temperature and characteristic high pressure gradient support the interpretation that the region between the clusters is a shock front (Mason et al. 2010). RXJ1347 also hosts a radio mini-halo centered on its primary cluster. While gas sloshing causes electron re-acceleration in the mini-halo, (Mazzotta & Giacintucci 2008), Ferrari et al. (2011) used observations by the Giant Metrewave Radio Telescope at 237 MHz and 614 MHz to find that excess radio emission in the southeast section of the mini-halo is likely caused by a propagating shock front corresponding to the shock-heated gas and SZ decrement previously found.

At a redshift of $z = 0.451$, RXJ1347 is close enough that the disturbed X-ray morphology resulting from recent mergers can be observed in detail with the high angular resolution of the *Chandra* X-ray Observatory. At this high angular resolution, our combined 186 ks *Chandra* exposure ( $> 2.5$ times deeper than previous *Chandra* observations) allows us to identify features not seen before, to better constrain the ICM gas hydrodynamics and, by comparison with simulations, RXJ1347's merger history. In §2 we discuss our reduction of the observational data and general analysis techniques. In §3 we analyze the mean and asymmetric gas properties in the primary cluster. We discuss the properties of the merging subcluster in §4, and we compare our results to simulations in §5 to discern the cluster merging history.

For the standard $\Lambda$ dominated cold dark matter cosmology and assuming $H_0 = 70\,\mathrm{km\,s^{-1}\,Mpc^{-1}}$, $\Omega_m = 0.3$, $\Omega_\Lambda = 0.7$, the redshift $z = 0.451$ for RXJ1347.5-1145 corresponds to a luminosity distance of 2504 Mpc and angular scale $1'' = 5.77$ kpc (Wright 2006). All WCS coordinates are J2000, and uncertainties are at 90% CL unless otherwise specified.

## 2. OBSERVATIONS AND DATA REDUCTION

In Table 1 we list the data sets used in this analysis. All observations were taken by the Advanced CCD Imaging Spectrometer (ACIS Garmire et al. 1992; Bautz et al. 1998) on board the *Chandra* X-ray Observatory with the ACIS-I array at aim point. Using the *Chandra* Interactive Analysis of Observations suite of analysis tools (CIAO 4.6 Fruscione et al. 2006) and CALDB 4.6.1.1, the data were reprocessed with the latest calibrations including updated gains and observation dependent bad pixel files, and corrections for the charge transfer inefficiency on the ACIS CCDs, the time-dependent build-up of contaminant on the optical filter, and the secular drift of the average pulse-height amplitude for photons of fixed energy (tgain). The data were then filtered to reject bad array patterns (grades 1, 5, and 7), and to remove data flagged by the VFAINT mode as having excessive counts in border pixels surrounding event islands. Particle flares were cleaned from the data with the tool *lc_clean*, using a $3\sigma$ clipping algorithm to calculate the mean count rate in the $0.3-12$ keV energy band, and then rejecting time periods in which the count rate fell more than 20% above or below the mean. These effective exposure times for each observation are listed in Table 1, resulting in a combined useful exposure for our analysis of 186,165 s.

TABLE 1
*Chandra* X-RAY OBSERVATIONS

| ObsID | Exposure Time (ks) | Bkg Norm | Date | PI |
|---|---|---|---|---|
| 3592 | 49.643 | 0.870 | 2003−09−03 | L. van Speybroeck |
| 14407 | 56.076 | 0.769 | 2012−03−16 | C. Jones |
| 13999 | 47.817 | 0.842 | 2012−05−14 | C. Jones |
| 13516 | 32.629 | 0.772 | 2012−12−11 | S. Murray |

NOTE. — *Chandra* observations used in this analysis. All observations were taken in VFAINT mode with ACIS-I at aim point. Column 2 lists the effective exposure after excluding periods of anomalously high and low count rates (see §2). Column 3 lists the additional normalization needed for blank sky backgrounds to match the observation count rate in the $10-12$ keV energy band.

Source free background sets, provided by the Chandra X-ray Center, appropriate for the ACIS-I detector and date of observation, were reprojected onto each observation, and renormalized to match the observation count rate in the $10-12$ keV energy band where particle backgrounds dominate. These additional normalization factors are also listed in Table 1. Background subtracted, exposure corrected mosaiced X-ray surface brightness images were then created in various energy bands using the CIAO script *flux_image* and other CIAO tools.

We used the broad band ($0.5-7$ keV) mosaiced X-ray surface brightness image to identify 'by eye' 77 point sources in the combined field of view. Since we are interested in the properties of the diffuse emission from the cluster gas, these sources were excised from the data. We compared our point source list to that given in the Chandra Source Catalog (Evans et al. 2010) for this region, and found that our removal of point sources was more conservative. We also excluded from our analysis a linear artifact (read-out streak), seen in the mosaiced image to extend from the bright X-ray peak at the cluster center to the northeast and southwest (at 110° and 290°, respectively, measured counter-clockwise from west). Since we are interested in the properties of the diffuse emission in the cluster rather than the central bright source, excluding this artifact will not affect our results.

## 3. PRIMARY CLUSTER

The 186 ks *Chandra* background subtracted, exposure corrected, combined $0.5-2.5$ keV full resolution X-ray surface brightness image is displayed in Figure 1. We used the $0.5-2.5$ keV energy band for imaging analysis, even though the cluster is hot, because of lower signal to noise in the higher ($2.5-7.0$ keV) energy bands. The asymmetries in the surface brightness suggest the presence of dynamic, complex gas motions in both the primary cluster and merging subcluster. The subcluster is visible southeast of the primary cD galaxy, with its X-ray peak $\sim 22''$ distant from the primary cluster BCG, as seen in previous X-ray and SZ observations (see, e.g. Johnson et al. 2012; Komatsu et al. 2001; Kitayama et al. 2004; Ota et al. 2008). In this section we focus on the

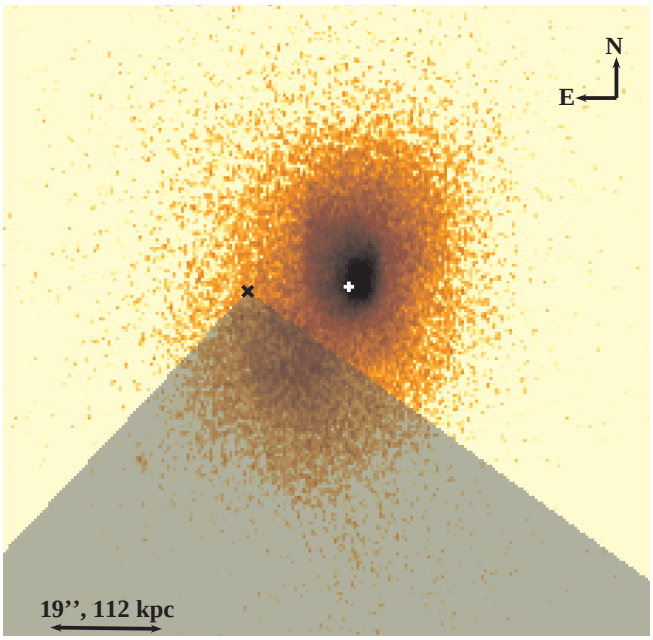


FIG. 2.— We show the flux image from Figure 1 with a mask covering the region excluded from the mean primary cluster gas distribution fit. The figure has a log scale with the primary (subcluster) cD galaxy labeled as a white cross (black X).

properties of the primary cluster gas, deferring the discussion of the subcluster to Section 4. Edges in the surface brightness trace a spiral feature in the primary cluster. We have noted these edges, as well as the centers of the primary and subcluster cD galaxies in Figure 1. To understand these gas asymmetries in the primary cluster, we begin with an analysis of its mean gas distribution.

### 3.1. *Gas Distribution*

We use *Sherpa* to fit a 2 dimensional elliptical beta model of surface brightness to the RXJ1347 0.5−2.5 keV full resolution (1 pixel= 0.″492) counts image:

$$S_x(r) = A\left[1+\left(\frac{r}{r_0}\right)^2\right]^{-\alpha} \quad (1)$$

with

$$r(x,y) = \frac{\sqrt{x_{new}^2(1-\epsilon)^2+y_{new}^2}}{1-\epsilon} \quad (2)$$

$$x_{new} = (x-x_0)\cos(\theta)+(y-y_0)\sin(\theta) \quad (3)$$

$$y_{new} = (y-y_0)\cos(\theta)-(x-x_0)\sin(\theta) \quad (4)$$

and where $x_0$ and $y_0$ are the coordinates of the X-ray peak, A is the amplitude at $x_0$ and $y_0$, $\epsilon$ is ellipticity, $\theta$ is the angle of ellipticity, $r_0$ is the core radius, and $\alpha$ is the power law index. An exposure map for the full resolution 0.5−2.5 keV image was included in the fit.

To obtain parameters descriptive of only the primary cluster rather than the system with both clusters, a sector covering the subcluster centered on the second brightest cluster galaxy (RA $13^h47^m31.9^s$, Dec $-11°45'10.''9$) spanning an angle of 227° to 324° counterclockwise from west was excluded from the image using CIAO tools (see Figure 2). The sector's size was chosen given the cone-like appearance of the subcluster in Figure 1. We choose to exclude the subcluster's gas contribution rather than jointly fit both clusters' distributions because there is little diffuse subcluster gas contribution to the primary cluster outside the cone surrounding the subcluster. Parameters for modeling the masked image were found by first using *Sherpa*'s Monte Carlo optimization method with the Cash statistic to roughly locate the global minimum (Cash 1979; Storn & Price 1995). The Levenberg-Marquardt minimization technique was then used with the Monte Carlo best-fit as starting points to precisely locate the minimum (Moré 1978). Core radius $r_0$, $x_0$ and $y_0$ positions, ellipticity $\epsilon$, angle of ellipticity $\theta$, amplitude $A$, and model power law index $\alpha$ were allowed to vary simultaneously during each minimization. Parameters for the best fit are listed in Table 2.

TABLE 2
2 DIMENSIONAL ELLIPTICAL BETA MODEL PARAMETERS: PRIMARY CLUSTER

| Parameter | Best-Fit | Lower Bound | Upper Bound |
|---|---|---|---|
| $r_0$ | 5.1 | −0.1 | 0.04 |
| A | $1.6\times10^{-6}$ | $-1.6\times10^{-8}$ | $4.5\times10^{-8}$ |
| $\alpha$ | 1.12 | −0.005 | 0.004 |
| $x_0$ | 13 : 47 : 30.7 | −0.01 | 0.1 |
| $y_0$ | −11 : 45 : 08.1 | −0.03 | 0.1 |
| $\epsilon$ | 0.2 | −0.005 | 0.006 |
| $\theta$ | 88 | −1 | 1 |

NOTE. — Best-fit *Sherpa* parameters with uncertainties for the primary cluster fit. $x_0$ and $y_0$ are given in RA, Dec. Core radius and its uncertainties, as well as $x_0$ and $y_0$ uncertainties, are in arcsec, while amplitude (A) is in photons $pix^{-1}$ $cm^{-2}$ $s^{-1}$. $\alpha$ and $\epsilon$ are unitless, and $\theta$ has units of degrees. Uncertainties for the fit are 90% CL.

We can find the value of the familiar $\beta$ parameter by equating $\alpha = 3\beta - 1/2$ (Jones & Forman 1984). Given the best-fit $\alpha$ value of 1.12, $\beta = 0.54$ for a core radius of $r_0 = 29.4^{+0.2}_{-0.6}$ kpc. The average gas density can be modeled using our $\beta$ value:

$$n_{gas}(r) = n_{gas}(0)\left[1+\left(\frac{r}{r_0}\right)^2\right]^{-3\beta/2} \quad (5)$$

Our mean $\beta$-model fit agrees well with that found by Allen et al. (2002) ($\beta = 0.535\pm0.003$, $r_0 = 29.2\pm0.7$ kpc), from fitting the 0.3−7 keV image excluding the southeast subcluster quadrant. Previous shallower observations by Allen et al. (2002) and Gitti et al. (2007) found that the cluster appears, on average, symmetric and relaxed. Our model shows a small elongation in the N-S direction, consistent with qualitative features seen in the deep X-ray image in Figure 1.

### 3.2. *Characterization of Gas Asymmetries*

Displacement of the X-ray surface brightness peak to the west of the primary cluster cD galaxy indicates the core has most recently sloshed to the west (see Figure 1). We show a projected temperature map in the left panel of Figure 3. The temperature map was created by growing regions around each pixel in the 0.6−9 keV mosaiced image until the region contained at least 3000 counts. The spectrum was then fit with an absorbed APEC model with Galactic absorption and Anders & Grevesse (1989) abundance fixed at $0.5\,Z_\odot$ (Ota et al. 2008). $1\sigma$ uncertainties in the fits range from 8% for tempera-

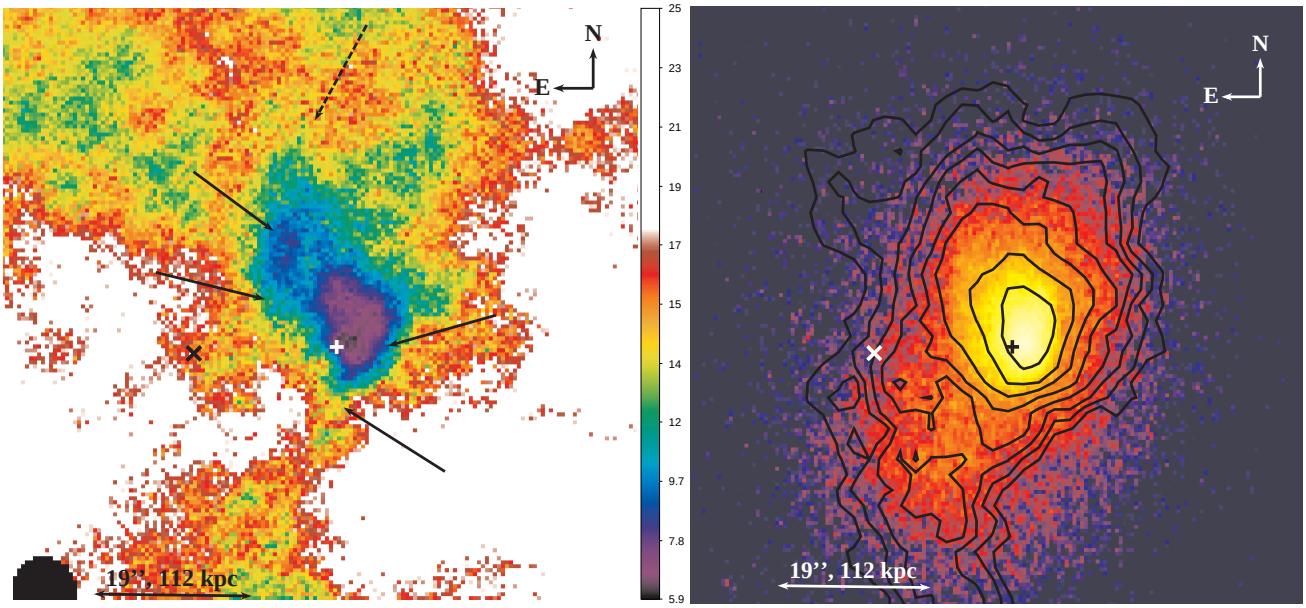


FIG. 3.— (Left) Temperature map of RXJ1347. The rainbow color scale increases in temperature from black (lowest) to white (highest) in keV. The black circle is a removed point source. Arrows point to the cold fronts labeled in Figure 1. The fan region is shown by a dashed arrow. $1\sigma$ uncertainties in the fits range from 8% for temperatures $\sim 6.5$ keV in the core to $25-30$% for temperatures $\gtrsim 20$ keV in the cluster outskirts. (Right) Entropy contours overlaid on the full resolution combined flux image from Figure 1 matched in WCS coordinates to the temperature map. Low entropy contours trace the cold fronts and fan that form part of the spiral. The +(X) symbol denotes the primary cluster (subcluster) BCG, respectively, in both panels.

TABLE 3
PRIMARY CLUSTER COLD FRONT PROFILE REGIONS

| Region | Semi-Minor Axis (arcsec) | Semi-Major Axis (arcsec) | Position Angle (deg) | Angle A (deg) | Angle B (deg) |
|---|---|---|---|---|---|
| West | 5.1 | 8.5 | 74 | 315 | 42 |
| Southeast | 6.2 | 8.4 | 137 | 183 | 275 |
| East | 6.8 | 16.3 | 107 | 127 | 152 |
| Northeast | 6.6 | 24.0 | 99 | 109 | 127 |

NOTE. — Bounding ellipses trace sector edges. All sectors were centered at primary cD RA 13 : 47 : 30.7, Dec −11 : 45 : 10.1 and subtend the angle from A to B, moving counter-clockwise from west. Position angles are defined as the angle between the semi-major axis and west.

TABLE 4
COLD FRONT BROKEN POWER MODEL PARAMETERS

| Region | Inner Slope | Outer Slope | Location of Edge (arcsec) | $\frac{\rho_2}{\rho_1}$ | $\frac{T_2}{T_1}$ | $\frac{P_2}{P_1}$ |
|---|---|---|---|---|---|---|
| West | $-0.65^{+0.10}_{-0.08}$ | $-1.14^{+0.05}_{-0.04}$ | $5.85^{+0.04}_{-0.03}$ | $1.80^{+0.10}_{-0.08}$ | $0.56^{+0.16}_{-0.13}$ | $1.00^{+0.29}_{-0.24}$ |
| Southeast | $-0.78 \pm 0.09$ | $-0.72^{+0.06}_{-0.05}$ | $7.10^{+0.07}_{-0.03}$ | $1.62^{+0.15}_{-0.13}$ | $0.65^{+0.29}_{-0.22}$ | $1.06^{+0.48}_{-0.37}$ |
| East | $-0.53 \pm 0.08$ | $-1.36^{+0.06}_{-0.14}$ | $11.5^{+1.3}_{-1.2}$ | $1.51^{+0.11}_{-0.21}$ | $0.66^{+0.48}_{-0.24}$ | $0.99^{+0.73}_{-0.39}$ |
| Northeast | $-0.76 \pm 0.04$ | $-1.57 \pm 0.06$ | $16.7^{+0.3}_{-0.5}$ | $1.44 \pm 0.09$ | $0.58^{+0.27}_{-0.16}$ | $0.83^{+0.39}_{-0.24}$ |

NOTE. — Parameters correspond to the best-fit density model for the elliptical profiles. $\rho_1$, $T_1$, and $P_1$ refer to the density, temperature, and pressure outside the cold front, and $\rho_2$, $T_2$, and $P_2$ represent the density,temperature, and pressure inside the cold front. Uncertainties are presented at 90% confidence. Temperatures were fit on each side of the edges (see Table 7).

TABLE 5
SPECTRAL LOCAL BACKGROUND REGIONS

| ObsID | $x_0$ RA | $y_0$ dec |
|---|---|---|
| 13516 | 13 : 47 : 41.1 | −11 : 44 : 05.2 |
| 3592 | 13 : 47 : 41.1 | −11 : 44 : 05.2 |
| 13999 | 13 : 47 : 40.4 | −11 : 44 : 46.9 |
| 14407 | 13 : 47 : 39.1 | −11 : 43 : 59.3 |

NOTE. — Unrotated rectangles with sides of 39.″9 and 38.″9 were used as local backgrounds when extracting spectra from regions.

tures $\sim 6.5$ keV in the core to 25−30% for temperatures $\gtrsim 20$ keV in the cluster outskirts.

The temperature map in Figure 3 shows complicated structures. A temperature dip west of the primary BCG indicates the sloshing core's presence. High temperatures in the southwest and southeast at large radii (the white regions in Figure 3) relative to temperatures at similar radii to the north and northeast could be due to shock heating from a previous encounter.

Wrapping around the primary BCG in the X-ray flux image is a clockwise spiral that is elongated to the north. We denote these spiral edges in Figure 1. Both the west and east cold fronts identified by Johnson et al. (2012) form part of the spiral. Edges in the projected temperature image align well with those in the X-ray flux image (see arrows in Figures 1 and 3). In the right panel of Figure 3, we overlay pseudo-entropy ($s = TS_X^{-1/3}$) contours on the flux image. The contours show low entropy gas in the primary cluster core that traces the cold fronts. A diffuse, cool fan extends from the northeastern spiral elongation in both the temperature and flux images. The low entropy contours also elongate along this fan feature. However, the temperature map is coarse, giving only a qualitative picture of the complicated temperature structure in the cluster and serving as a guide for more careful spectral modeling of regions of interest.

### 3.3. *Cold Fronts*

Elliptical surface brightness profiles of the combined, background subtracted, exposure corrected 0.5−2.5 keV full resolution flux image were taken to characterize edge properties. The profiles were taken in four sectors, each centered on the primary cluster BCG, based on features seen in the X-ray and temperature images described in §3.2. The ellipses used to construct the profiles were chosen congruent to a bounding ellipse that traces the edge in each sector. See Table 3 for parameters defining each sector and the bounding ellipses used to trace the edges in each sector.

We integrate a broken power law model of density along the line of sight to fit the elliptical surface brightness profiles across each edge. The density model is given by:

$$n_{gas}(r) = n_{e,0}\frac{\rho_2}{\rho_1}\left(\frac{r}{r_s}\right)^{\nu_2} \qquad \text{for } r < r_s \qquad (6)$$

$$n_{gas}(r) = n_{e,0}\left(\frac{r}{r_s}\right)^{\nu_1} \qquad \text{for } r > r_s \qquad (7)$$

where $n_{e,0}$ is the overall normalization, $\frac{\rho_2}{\rho_1}$ is the density ratio between the inner and outer power law slopes, $r_s$ is the location of the edge, and $\nu_2$ and $\nu_1$ are the inner and outer power law slopes, respectively. Results of our fits are summarized in Table 4.

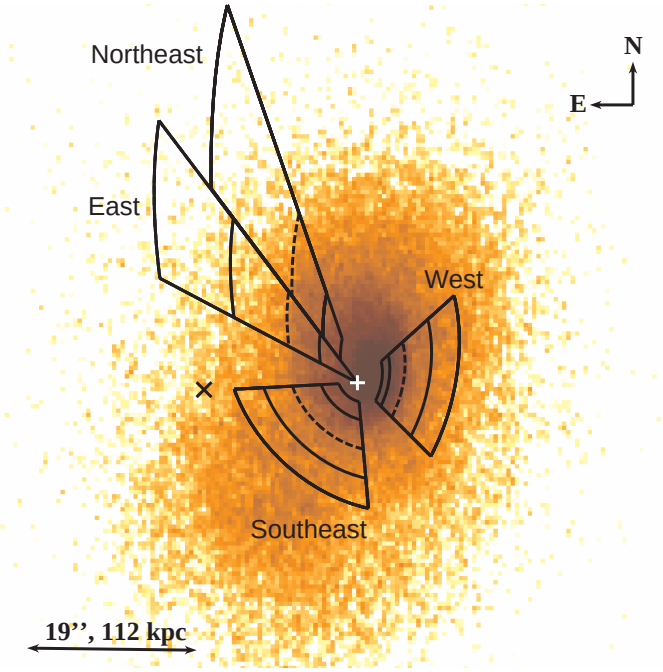


FIG. 4.— Sectors used to extract the elliptical surface brightness profiles plotted in the top panel of Figure 5 overlaid on the full resolution flux image of RXJ1347 from Figure 1. Regions used for spectral analysis are shown as elliptical arcs concentric to the bounding ellipses (long dashed lines) listed in Table 3 that trace the observed surface brightness edges within each sector.

We extracted spectra for regions of interest using CIAO script *specextract* and chose $39.''9 \times 38.''9$ rectangular source free regions on the ACIS-I array as local backgrounds for each observation (see Table 5). Spectra from each of the four observations were fit together, but extracted separately for each region. Except where noted, we required a minimum of 2000 net counts total to constrain the expected high gas temperatures in this cluster. Spectra of diffuse gas were modeled in XSpec 12.8.0, using absorbed APEC models (Smith et al. 2001) with fixed Galactic absorption $n_H = 4.75 \times 10^{20}$ cm$^{-2}$ (Leiden/Argentine/Bonn collaboration, Snowden et al. 1997) and abundance at $0.5 Z_\odot$ (Ota et al. 2008). See Tables 5 and 6 for cold front spectral region parameters and Table 7 for temperature values. Spectral regions are also shown within sectors in Figure 4.

Surface brightness, density, temperature, and pressure profiles for the west, southeast, east, and northeast elongated edges are plotted in Figure 5. We find the west edge is well described by a density jump of $1.80^{+0.10}_{-0.08}$ and temperature jump of $0.56^{+0.16}_{-0.13}$ located $5.''85^{+0.04}_{-0.03}$ west of the primary cluster cD galaxy. These measurements yield a pressure jump of $1.00^{+0.29}_{-0.24}$ across the edge. We find similar density, temperature, and pressure jumps across the southeast, east, and northeast edges located at $7.''10^{+0.07}_{-0.03}$, $11.''5^{+1.3}_{-1.2}$, and $16.''7^{+0.3}_{-0.5}$ from the primary cluster cD galaxy, respectively (see Table 4). Our density, temperature, and pressure ratios show that all of these edges are consistent with sloshing cold fronts. Our east and west cold fronts agree well with those found by Johnson et al. (2012). Small differences in edge radii and jump values are due partly to our longer exposure, and also to differences in binning, density model, and the geometry and centering used

TABLE 6
COLD FRONT SPECTRAL REGIONS

| Sector | Semi-Minor Axis Out (arcsec) | Semi-Major Axis Out (arcsec) | Semi-Minor Axis In (arcsec) | Semi-Major Axis In (arcsec) |
|---|---|---|---|---|
| W3 | 3.50 | 5.81 | 2.70 | 4.49 |
| W2 | 5.14 | 8.53 | 3.50 | 5.81 |
| W1 | 8.00 | 13.38 | 5.14 | 8.53 |
| W0 | 11.00 | 18.25 | 8.00 | 13.38 |
| SE3 | 3.68 | 5.01 | 1.88 | 2.56 |
| SE2 | 6.60 | 8.99 | 3.68 | 5.01 |
| SE1 | 9.50 | 12.94 | 6.60 | 8.99 |
| SE0 | 12.50 | 17.03 | 9.50 | 12.94 |
| E3 | 3.69 | 8.82 | 0 | 0 |
| E2 | 6.82 | 16.32 | 3.69 | 8.82 |
| E1 | 12.3 | 29.41 | 6.82 | 16.32 |
| E0 | 19.68 | 47.06 | 12.3 | 29.41 |
| NE3 | 3.48 | 12.65 | 1.72 | 6.26 |
| NE2 | 6.61 | 24.04 | 3.48 | 12.65 |
| NE1 | 14.76 | 53.68 | 6.61 | 24.04 |

NOTE. — Elliptical segments are restricted to lie within each sector and are congruent to the bounding ellipse that traces the edge within the sector (see Table 3).

TABLE 7
COLD FRONT TEMPERATURES

| Sector | Temperature (keV) | $\chi^2$/(d.o.f.) |
|---|---|---|
| W3* | $5.9^{+1.0}_{-0.8}$ | 75.75/84 |
| W2 | $7.4^{+1.0}_{-0.9}$ | 204.80/143 |
| W1 | $13.3^{+3.3}_{-2.7}$ | 166.91/145 |
| W0 | $13.6 \pm 2.7$ | 130.17/135 |
| SE3* | $12.8^{+4.9}_{-3.4}$ | 81.48/84 |
| SE2 | $13.8^{+3.6}_{-3.0}$ | 169.14/156 |
| SE1 | $21^{+8}_{-5}$ | 110.78/130 |
| SE0 | $20^{+7}_{-4}$ | 173.42/151 |
| E3† | $11.9^{+5.8}_{-3.2}$ | 62.31/69 |
| E2* | $10.7^{+3.8}_{-2.2}$ | 82.01/83 |
| E1* | $16.2^{+10.3}_{-4.7}$ | 82.22/77 |
| E0† | $9.7^{+4.4}_{-2.3}$ | 51.67/67 |
| NE3† | $9.0^{+3.5}_{-1.9}$ | 80.16/66 |
| NE2⋆ | $8.9^{+2.4}_{-1.5}$ | 98.93/100 |
| NE1⋆ | $15.4^{+5.8}_{-3.5}$ | 97.56/103 |

NOTE. — Temperatures are presented with 90% CL after being fit with fixed Galactic absorption and abundance at $0.5 Z_{\odot}$. Labels of W, SE, E, and NE correspond to temperatures in the West, Southeast, East, and Northeast profiles. Numerical labels of 3, 2, 1, and 0 correspond to the most inward sector, the sector just inside of the cold front, the sector just outside the cold front, and the sector farthest from the primary BCG. We use the following symbols to denote the combined number of net counts: †: >1000 counts, ∗: >1500 counts, and ⋆: >2000 counts. Unlabeled sectors have more than 2500 net counts.

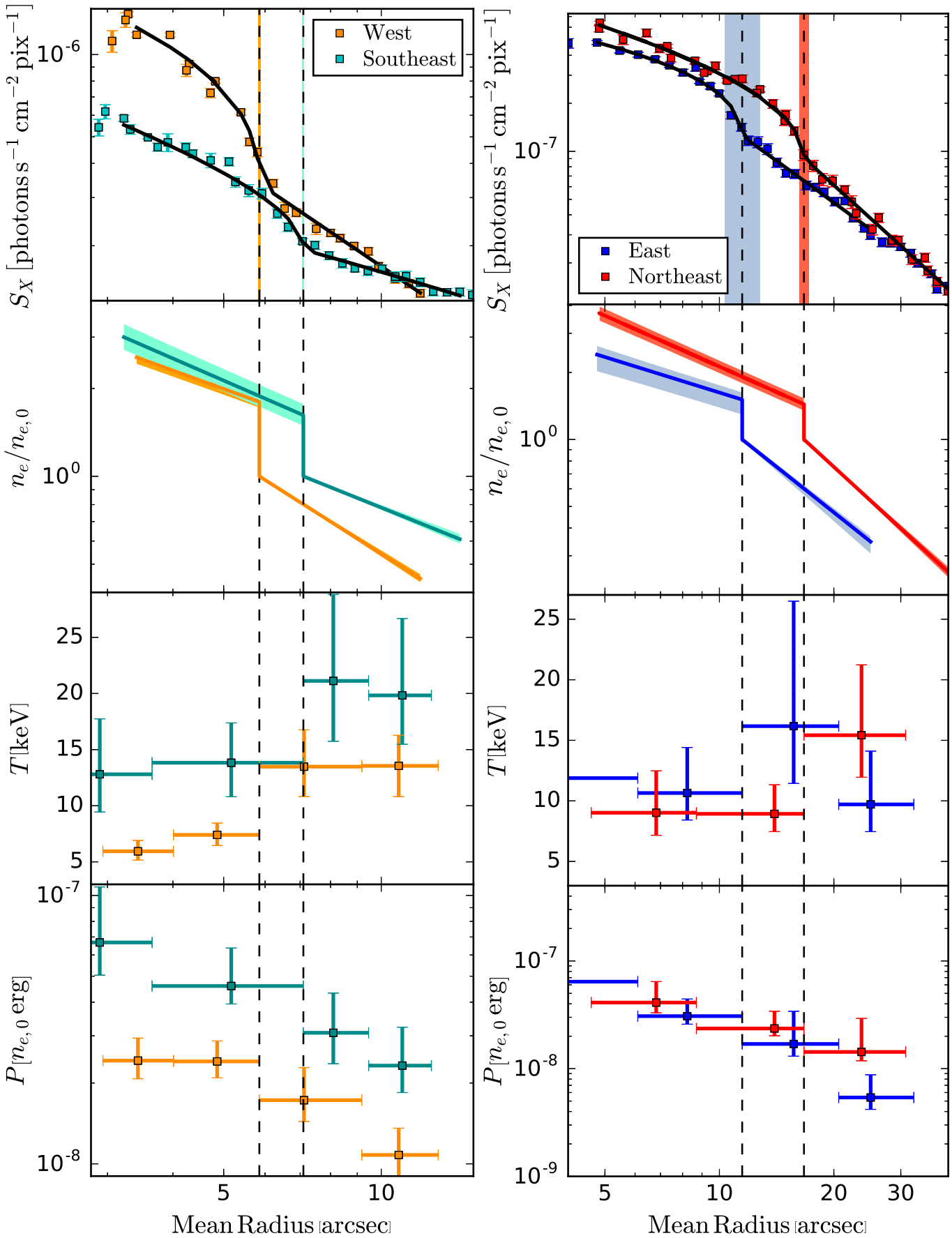


FIG. 5.— Surface brightness profiles, best-fit density profiles, temperature profiles, and pressure profiles are displayed for the 4 identified cold fronts. The left panel shows the west and southeast fronts, while the right panel displays the east and northeast fronts. Edge locations for the fronts are denoted by a vertical dashed line. Uncertainties in the edge fit parameters are colored to correspond to the relevant profiles. Best-fit parameters are in Table 4.

to extract the profiles.

The cold fronts we have measured agree with the edges identified visually in the images in §3.2. The radial distance between the cold fronts and the primary cluster cD galaxy gradually increases while rotating clockwise from west. This pattern is characteristic of a clockwise gas spiral formed from gas sloshing. Cold fronts radially closer to the primary cluster cD galaxy were formed more recently than those farther away.

As an independent check on our edge identifications, we apply the Gaussian gradient magnitude (GGM) filter to the background subtracted, full resolution flux image (Figure 1), following the methodology in (Sanders et al. 2016a,b). This filter highlights edges by showing high values for large gradients and low values for flat surface brightness profiles. In Figure 6 we show filtered images using standard deviations $\sigma$ of 1 pixel (0.″492), 2 pixels (0.″984), and 3 pixels (1.″476) in the top, middle, and bottom panels, respectively. A smaller $\sigma$ will highlight small scale gradients, while a larger $\sigma$ will highlight broad features. In the top and middle panels we have overlaid the 4 solid arrows denoting cold fronts seen in Figure 1. These arrows coincide with sharp gradients in the map, confirming our edge identifications and clockwise spiral feature. Filtering with $\sigma = 1$, the cold fronts appear to be traced by filamentary structures, possibly similar to those in the Centaurus cluster discussed by Sanders et al. (2016b). The bright central region likely corresponds to the bright, cool core in Figures 1 and 3. In the middle panel of Figure 6 ($\sigma = 2$), the cold front spiral is even more prominent. The elbow-like feature seen to the north in the top two panels is likely associated with the cooler, lower entropy northern fan extension noted in Figure 3.

## 4. SUBCLUSTER PROPERTIES

In Figure 1 excess X-ray emission, interpreted as gas from a merging subcluster, is seen to the southeast of the primary cluster. To better isolate the subcluster and study the X-ray morphology of its excess emission, we subtract the mean cluster model obtained in Section 3.1 for the primary cluster alone from the merged 0.5-2.5 keV X-ray image of the merging pair. This X-ray surface brightness difference map is given in Figure 7.

### 4.1. *Qualitative Features: the Case for Gas Stripping and Core Shredding*

Several qualitative features in Figure 7 are striking. The northern edges of the subcluster appear cone-like with the vertex displaced $\sim 2''$ south of the second BCG (taken to be the subcluster's central dominant galaxy), suggestive of gas displaced from the subcluster gravitational potential by ram pressure as it infalls through the primary cluster ICM from the southwest to the northeast. The western edge of this cone is in close correspondence to the maximum SZ decrement, as shown in the right panel of Figure 7 (Mason et al. 2010; Korngut et al. 2011), characteristic of a shock, suggesting that the cone-like feature may be the Mach cone of shocks formed by the subcluster's supersonic motion through the primary cluster ICM. Within the Mach cone is a bright region suggestive of the subcluster's gas core. The peak of the X-ray emission, defined as the brightest subcluster pixel in the 0.5−2.5 keV X-ray image shown in Figure 1, is located at RA $13^h47^m31.5^s$, Dec $-11°45'23.''7$. The morphology of the excess X-ray emission is elongated towards the southwest with the hint of an extended tail, also qualitatively consistent with that expected

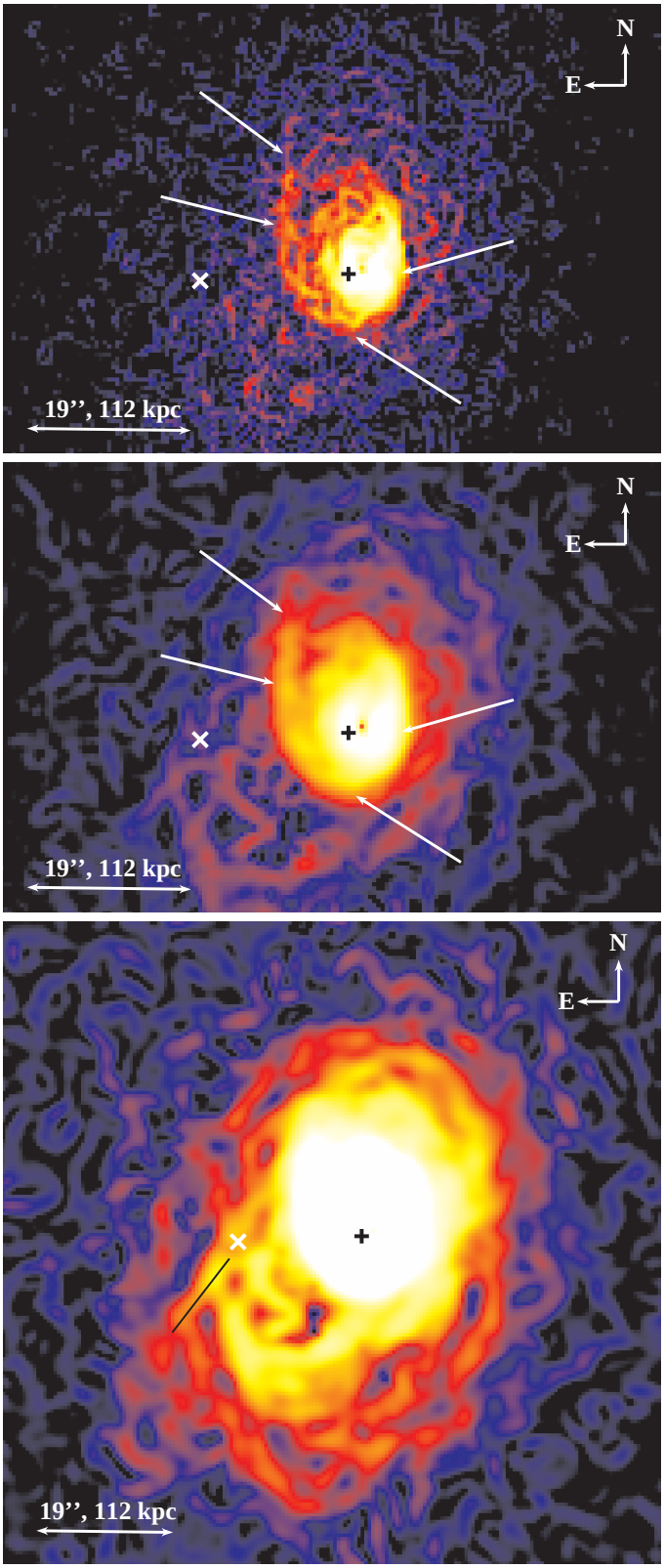


FIG. 6.— GGM filtered images using standard deviations $\sigma$ of 1 (top), 2 (middle), and 3 (bottom). The primary and subcluster BCGs are denoted by a cross and X, respectively. Solid arrows in the top and middle panels point to cold fronts labeled in Figure 1. In the bottom panel, the black line corresponds to the ellipse edge that traced the eastern shock front.

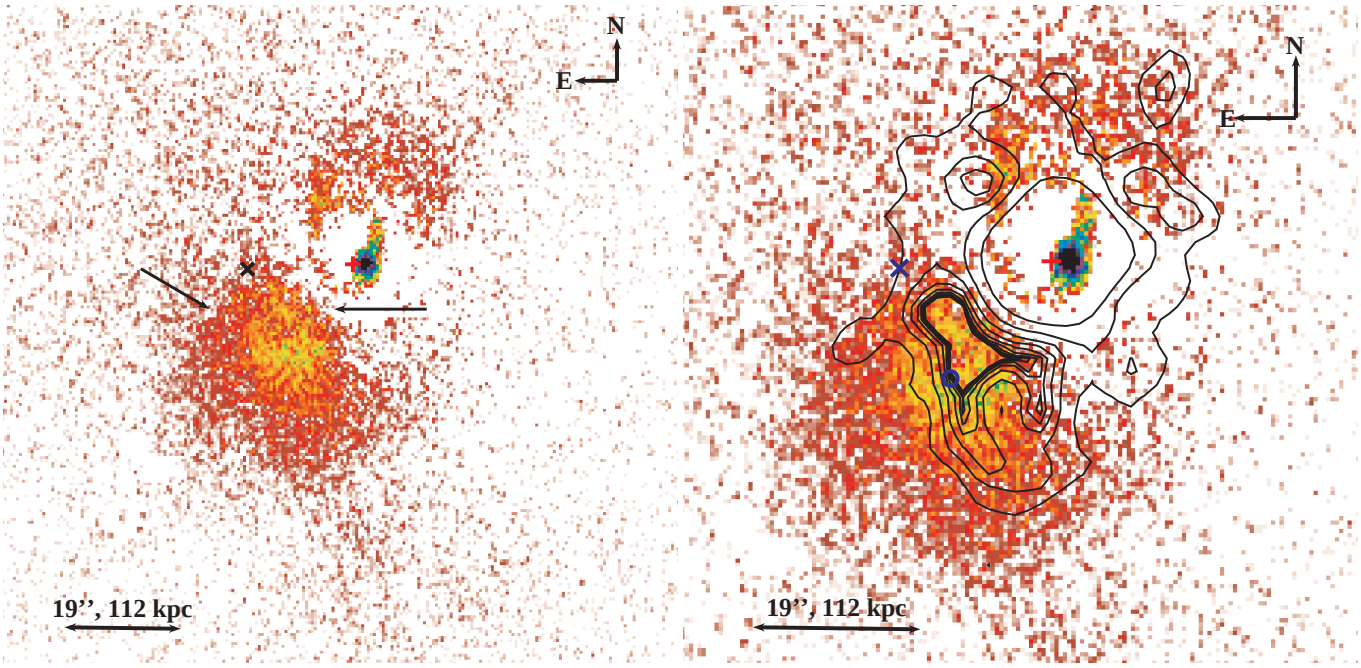


FIG. 7.— (Left) Difference map with log scale resulting from the residuals to the spherical beta model fit to the primary cluster surface brightness in §3.1. Note the prominence of the subcluster. We point to the sharp leading edges with arrows. (Right) Difference map with SZ contours overlaid, indicating the maximum SZ decrement over the western subcluster edge seen in the left panel, suggesting the edges represent the Mach cone of a shock front. The primary BCG, subcluster BCG, and subcluster X-ray peak are denoted with a cross, X, and circle, respectively.

for subcluster gas being stripped.

In Figure 8 we show pseudo-entropy contours overlaid on the surface brightness difference map (left panel) and temperature map (right panel) for the subcluster gas. Low entropy contours coincide with luminous, lower temperature regions in the subcluster and tail. We locate a 'ledge' in the southern contours, indicating an irregular distribution of low entropy gas in the elongated region. In a cluster whose core is still intact, we would expect a spherical entropy distribution with regular, monotonically increasing contours of entropy as a function of distance from the subcluster gas peak. While there is a concentration of low entropy gas near the subcluster X-ray surface brightness peak, the elongated, asymmetric entropy contours and lower temperatures to the southwest of the subcluster peak suggest ongoing core shredding as cooler core gas gas is pushed back towards the tail-like structure. These qualitative features are confirmed by the GGM $\sigma = 3$ map shown in the bottom panel of Figure 6. The eastern shock edge in the GGM image corresponds to the edge ellipse used for our shock density ratio analysis in §4.3 (see Figure 9). The western gradient edge corresponds to the SZ decrement. Together they trace the shock Mach cone. The bright extension to the southwest likely corresponds to the subcluster's stripped gas tail.

### 4.2. *Subcluster Temperature, Luminosity, and Mass*

To measure the temperature and luminosity of the subcluster, we extract the subcluster spectrum from a circular region of radius $11.''7$ located $22''$ from the primary cluster central galaxy, that covers the majority of the subcluster emission. To minimize the contribution to the spectrum from the primary cluster gas, we choose local background circles of the same size and distance from the primary cluster central galaxy as the subcluster, as in Johnson et al. (2012). However, the sloshing features (spiral and fan) cause the flux to vary with angle by as much as a factor of 2 at this distance (see Table 8 and Figure 10). We argue that the X-ray flux in the northern local background circle (BN in Figure 10) is anomalously high compared to that expected at the location of the subcluster due to this excess gas displaced to the north by sloshing. These sloshing features found to the north would not be expected at that radius in the southeast at the location of the subcluster. We instead fit the subcluster spectrum using the combined eastern (BE) and western (BW) cluster background regions as more representative of cluster emission at the location of the subcluster.

TABLE 8
CIRCULAR SUBCLUSTER AND BACKGROUND REGIONS

| Region | Center (RA), (Dec) | Flux (0.5 – 2.5 keV) $10^{-4}$ photons s$^{-1}$ cm$^{-2}$ |
|---|---|---|
| SC | 13 : 47 : 31.6, −11 : 45 : 27.4 | $1.716 \pm 0.016$ |
| BE | 13 : 47 : 32.1, −11 : 45 : 02.2 | $0.775 \pm 0.011$ |
| BN | 13 : 47 : 30.4, −11 : 44 : 48.7 | $1.491 \pm 0.015$ |
| BW | 13 : 47 : 29.2, −11 : 45 : 06.9 | $0.634 \pm 0.010$ |

NOTE. — SC includes emission from both the primary cluster and subcluster at $22''$ from the primary cluster central galaxy. BE, BN, and BW denote circular regions at the same radial distance containing primary cluster emission only. All circular regions have radius $11.''7$. Flux uncertainties are $1\sigma$.

Using an absorbed APEC thermal plasma model and fixing the absorbing column at the Galactic value ($4.75 \times 10^{-20}$ cm$^{-2}$), we find a subcluster temperature of $kT = 16^{+4}_{-3}$ keV (see Table 9) and abundance $A = 0.5^{+0.3}_{-0.2} Z_{\odot}$ ($\chi^2/\mathrm{dof} = 629/587$). From directly summing the 0.5 – 2.5 keV flux in the source and subtracting the expected primary cluster contribution using the BE+BW background regions, we measure an absorbed 0.5 – 2.5 keV flux for the subcluster alone of $1.01 \pm 0.02 \times 10^{-4}$ photons s$^{-1}$ cm$^{-2}$ ($1.96 \pm 0.03 \times$

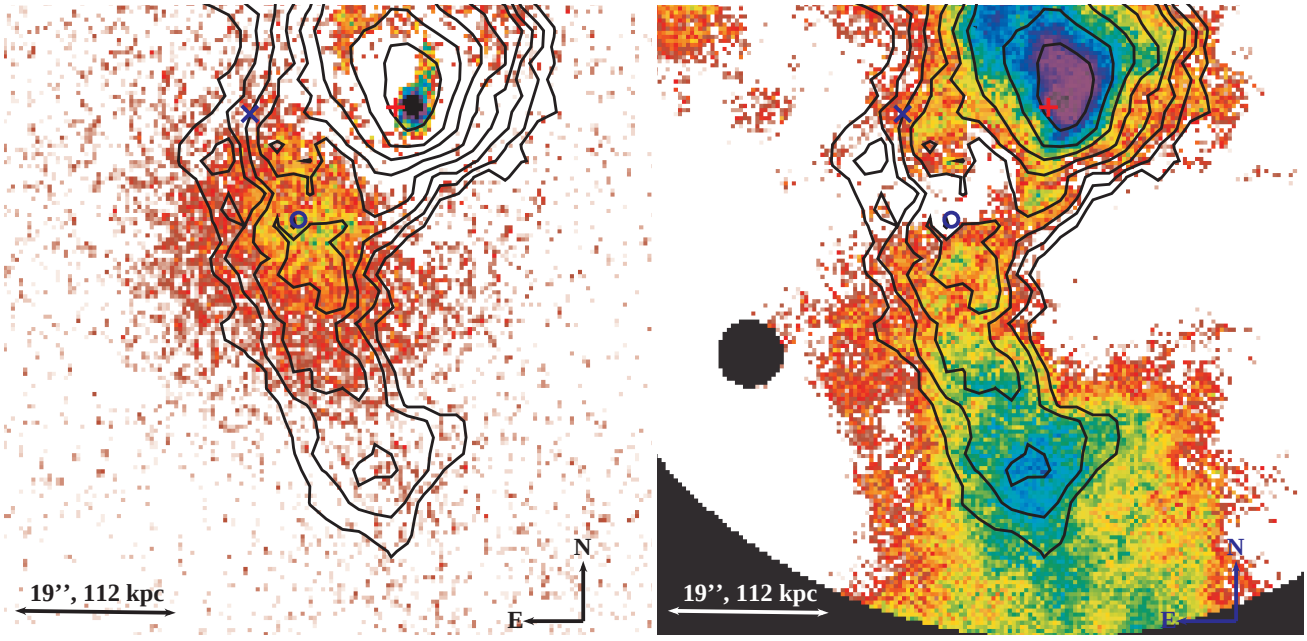


FIG. 8.— The left panel shows our difference map from Figure 7 with entropy contours overlaid while the right panel shows the same contours overlaid on the temperature map for the same region matched in WCS coordinates. The primary BCG, subcluster BCG, and subcluster X-ray peak are denoted with a red cross, blue X, and blue circle, respectively. The black circle in the temperature map is a removed point source.

TABLE 9
SUBCLUSTER TEMPERATURES

| Region | Temperature (keV) | $\chi^2$/(d.o.f.) |
|---|---|---|
| Total Subcluster Gas | $16^{+4}_{-3}$ | 621.66/588 |
| SZ Decrement | $19^{+6}_{-4}$ | 164.74/153 |

NOTE. — Temperatures are presented with 90% CL after being fit with an absorbed APEC model with fixed Galactic absorption and abundance at $0.3\,Z_{\odot}$.

$10^{-13}$ erg s$^{-1}$ cm$^{-2}$ ). While these $1\sigma$ statistical uncertainties are small given the long exposure, we caution the reader that the uncertainties in measuring the subcluster flux are dominated by the choice of model for the primary cluster emission at that location, and may be as high as $\sim 25\%$.

Our mean value for the net absorbed $0.5-2.5$ keV flux in the subcluster is higher (but still within their $1\sigma$ uncertainties) of that previously obtained by Johnson et al. (2012) ($1.5 \pm 0.9 \times 10^{-13}$ erg s$^{-1}$ cm$^{-2}$ ), because we exclude the northern region (BN) from our estimate of the average primary cluster emission and they did not. Using the spectral model to account for Galactic absorption and modest change in energy band to be consistent with Zhang et al. (2011), we find the unabsorbed $0.5-2$ keV X-ray luminosity of the subcluster to be $L_X = 1.3 \times 10^{44}$ erg s$^{-1}$ . Applying the $M_{gas,500} - L_{0.5-2keV,500}$ relationship from Zhang et al. (2011) for disturbed clusters including the core correction,

$$\log_{10}(Y) = A + B\log_{10}(X) \tag{8}$$

where

$$Y = \frac{L_{0.5-2keV,500}}{E(z)\ \mathrm{erg\ s^{-1}}} \tag{9}$$

$$X = \frac{M_{gas,500}E(z)}{10^{14}\ \mathrm{M_{\odot}}} \tag{10}$$

with $A = 44.44 \pm 0.61$, $B = 1.16 \pm 0.04$ at $1\sigma$, and

$$E^2(z) = \Omega_m(1+z)^3 + \Omega_\Lambda + (1-\Omega_m-\Omega_\Lambda)(1+z)^2 \tag{11}$$

we calculate the enclosed gas mass to be $3.3 \times 10^{13} M_{\odot}$. Assuming the gas fraction is 10% of the total mass (Vikhlinin et al. 2006), this yields the subcluster's total mass to be $3.3 \times 10^{14}$ M$_{\odot}$, consistent with the mass estimate found by Johnson et al. (2012). Since we expect that some subcluster gas may already have been stripped due to the encounter, this should be interpreted as a lower bound on the subcluster total mass.

### 4.3. *Eastern Shock Front and Shock Velocity*

Following the same procedure as in §3.3 with the $0.5-2.5$ keV full resolution exposure-corrected X-ray flux image, we construct the surface brightness profile across the eastern shock edge using elliptical wedge regions concentric to a bounding ellipse tracing the eastern shock edge and constrained to lie within the sector subtending the angles from 126° to 181°. The bounding ellipse is centered on the subcluster X-ray peak with semi-major (-minor) axes and position angle of 44″ (12″) and 51°, respectively (see Figure 9). We model the gas density using a broken power law density model across the subcluster eastern edge (see Equations 6 and 7, §3.3). To fit the surface brightness profile shown in the upper left panel of Figure 9, we integrate the square of the density model along the line of sight by using a multivariate $\chi^2$ minimization scheme. Our results for the best fit subcluster gas density ratio across the shock are shown in the lower left panel of Figure 9. We find the shock edge is located $13\farcs0^{+0.5}_{-0.3}$ northeast of the subcluster X-ray peak with a density ratio of $1.38^{+0.16}_{-0.15}$.

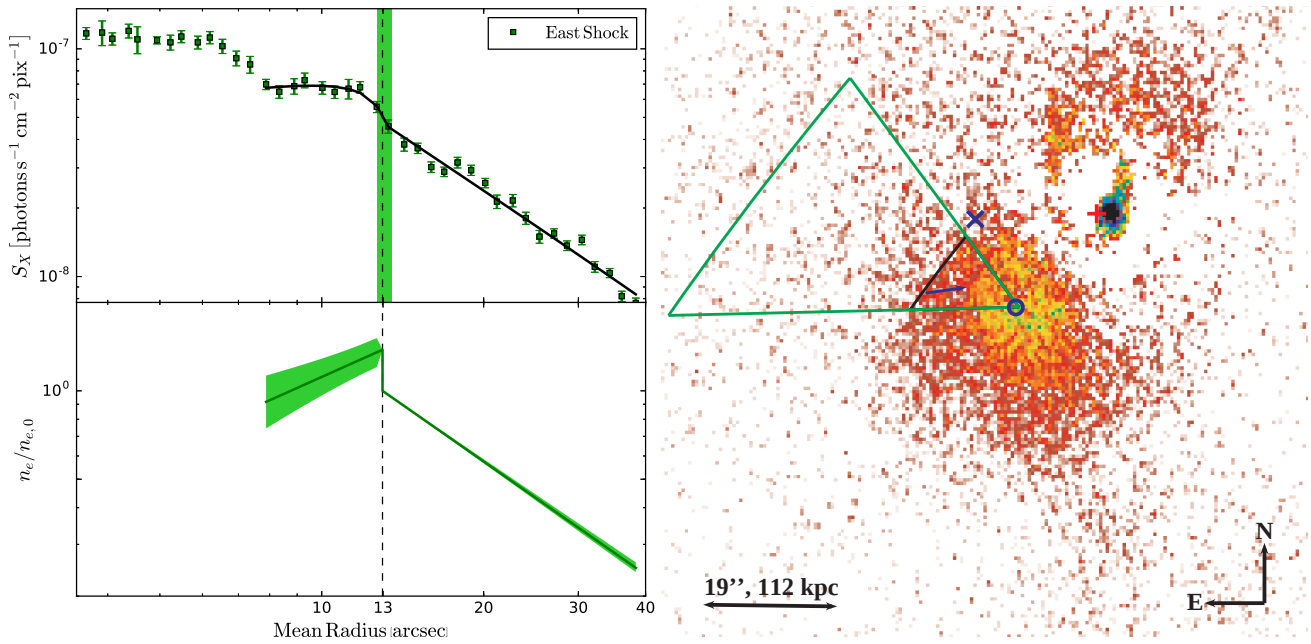


FIG. 9.— (Upper Left) The surface brightness profile across the eastern shock front. The black line shows the best fit assuming a broken power law (Equations 6 and 7) for the gas density. The potential merger cold front surface brightness jump is seen at $\sim 7-8''$. (Lower Left) Best fit gas density from the upper panel with power law indices $-1.28^{+0.04}_{-0.03}$ ($0.82^{+0.70}_{-0.59}$) upstream (downstream) of the shock. The shock edge location is denoted with a dashed line and 90% CL uncertainties shaded in green. (Right) The sector used to construct the surface brightness profile across the shock is overlaid on the residuals image with log scale. The black line shows the segment of the bounding ellipse that traces the eastern shock edge within the sector. The potential merger cold front surface brightness discontinuity is denoted with a blue arrow. See also the bottom panel of Figure 6.

TABLE 10
EASTERN SHOCK PROPERTIES

| Location of Edge (arcsec) | $\frac{\rho_{2,m}}{\rho_{1,m}}$ | $\frac{T_2}{T_1}$ | $\frac{P_2}{P_1}$ | Mach number | Velocity $\left(\mathrm{km\,s^{-1}}\right)$ |
|---|---|---|---|---|---|
| $13.0^{+0.5}_{-0.3}$ | $1.38^{+0.16}_{-0.15}$ | 1.25 | 1.72 | $1.25 \pm 0.08$ | $2810^{+210}_{-240}$ |

NOTE. — Shock properties were obtained by fitting a radial profile centered on the subcluster X-ray peak. Subscripts of 2 and 1 denote quantities downstream and upstream of the shock, respectively, whereas the subscript $m$ denotes a measured, rather than derived, quantity. $T_2/T_1$, $P_2/P_1$, and the Mach number were derived from the Rankine-Hugoniot jump conditions using the measured density ratio. The shock velocity assumes an unshocked gas temperature of $19 \pm 3$ keV.

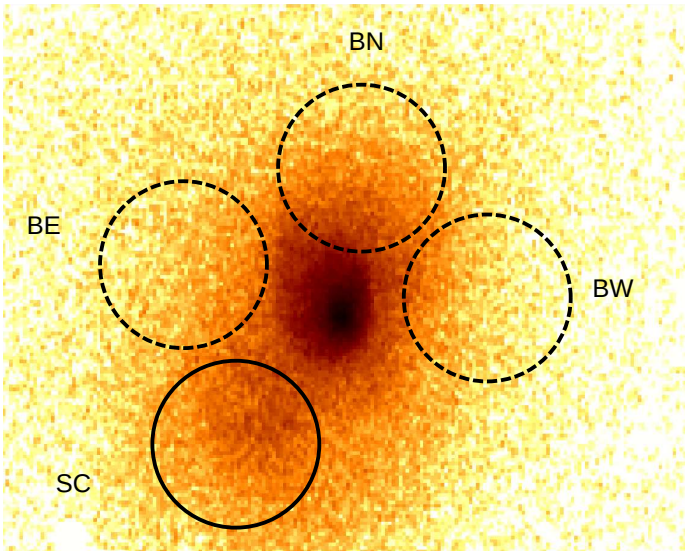


FIG. 10.— Source (subcluster + cluster, solid circle) and local background (cluster only, dashed circles) regions overlaid on the 0.5−2.5 keV flux image of RXJ1347. Note the excess emission in background region BN due to the northern extension of the spiral and fan.

The shock Mach number can be determined from either the density ratio $\rho_2/\rho_1$ or temperature ratio $T_2/T_1$ across the shock using the Rankine-Hugoniot jump conditions (Finoguenov et al. 2010; Korngut et al. 2011)

$$\mathcal{M}_\rho = \left[\frac{2\frac{\rho_2}{\rho_1}}{\gamma+1-(\gamma-1)\frac{\rho_2}{\rho_1}}\right]^{1/2} \quad (12)$$

and

$$\mathcal{M}_T = \left\{\frac{8\frac{T_2}{T_1}-7+\left[\left(8\frac{T_2}{T_1}-7\right)^2+15\right]^{1/2}}{5}\right\}^{1/2} \quad (13)$$

where $\gamma = \frac{5}{3}$, and $\rho_2$ ($T_2$) and $\rho_1$ ($T_1$) are the gas densities (temperatures) inside and outside the shock, respectively. Using our measured density ratio in Equation 12, we find a shock Mach number $M_\rho = 1.25 \pm 0.08$.

We calculate the velocity of the eastern shock by multiplying the Mach number by $c_s$, the speed of sound in the unshocked primary cluster plasma, using

$$c_s^2 = \frac{\gamma P_g}{\rho_g} \quad (14)$$

where

$$P_g = n_g k_B T_K \quad (15)$$

$$\rho_g = n_g \mu m_p \quad (16)$$

and $\gamma = \frac{5}{3}$ and $\mu = 0.6$. Thus,

$$c_s^2 = \frac{\gamma k_B T_K}{\mu m_p} = \frac{\gamma T_{eV}}{\mu m_p} \quad (17)$$

and

$$c_s = 516 \text{ km s}^{-1} T_{keV}^{1/2}. \quad (18)$$

Using the local background regions from Table 5, we extract a spectrum for region BE from Figure 10 and Table 8 to the north of the tip of the Mach cone (see Figure 7) to measure the temperature and determine the local sound speed in the cluster gas outside the shock. Modeling the spectrum with an absorbed APEC model with fixed Galactic absorption and abundance at $0.3\,Z_\odot$, we find a cluster gas temperature $kT = 19 \pm 3$ keV ($\chi^2/\text{dof} = 297/305$ for 7386 net source counts, see Table 9). From Equation 18, we estimate the speed of sound in the unshocked cluster gas as $c_s = 2250^{+170}_{-190}$ km s$^{-1}$ and eastern shock velocity of $2810^{+210}_{-240}$ km s$^{-1}$ .

From Equation 13, we predict a (deprojected) temperature ratio $T_2/T_1 = 1.25$. To test this prediction, one would ideally extract spectra in narrow regions on either side of the shock edge. However, we cannot measure the temperature jump in such regions to within 25% uncertainty with these data ($T_2 = 16^{+23}_{-7}$ keV and $T_1 = 14^{+26}_{-6}$ keV, yielding $T_2/T_1 = 1.2^{+2.7}_{-0.7}$). Although we find no significant difference between the temperatures of the subcluster and the cluster gas just outside the shock, the measured temperature ratio is consistent with the Rankine Hugoniot prediction within 90% CL uncertainties.

### 4.4. *Subcluster Cold Front?*

In the elliptical surface brightness profile across the eastern shock (Figure 9), we find a second jump in the surface brightness $\sim 5''$ closer to the subcluster X-ray peak than the shock front. The surface brightness discontinuity is small and gas temperatures are high and have a complex distribution, so measurements are highly uncertain, causing us to not complete a formal edge analysis. However, qualitatively the double-jump nature of this profile is reminiscent of the Bullet subcluster (see Markevitch et al. 2002). For the Bullet, the inner jump was a cold front between the subcluster core and outer gas. The concentration of low entropy gas near the X-ray peak for our subcluster suggests that there is still a remnant core, and that, as in the Bullet cluster, the inner surface brightness edge may correspond to a merger cold front.

### 4.5. *Western Shock Front*

As the subcluster merges with the primary cluster, gas is shock heated. High temperatures southwest of the subcluster cD galaxy suggest the presence of a western shock front (see right panel of Figure 11). SZ contours from a MUSTANG SZ map, provided by Mason et al. (2010) and smoothed by a $10''$ FWHM Gaussian, were overlaid on the difference map (left panel of Figure 11). The most significant SZ decrement over the subcluster occurs from $\sim 13''$ to $\sim 17''$ southeast of the primary cluster cD galaxy. We choose a rectangular region centered at RA, Dec = $13^h47^m31.4^s, -11°45'19.''5$ with long (short) sides of $12.''3$ ($4.''5$), respectively, oriented at position angle 130° along the most significant SZ decrement to study this region. Using an absorbed APEC model with fixed Galactic absorption, abundance fixed at $0.3Z_\odot$ and local backgrounds from Table 5, we find the temperature of the gas in this region to be $19^{+6}_{-4}$ keV ($\chi^2/\text{dof} = 165/174$). This region corresponds to the high temperature ridge between the subcluster and primary cluster in the right panel of Figure 11. A surface brightness profile centered on the primary cluster cD galaxy taken in the sector subtending the angles from 198° to 258° with semi-major (-minor) axes and position angle of $56''$ ($15''$) and 138°, respectively, traces the shape of the decrement as well as the proposed western shock front. The profile indicates increased surface brightness over the edge. See Fig-

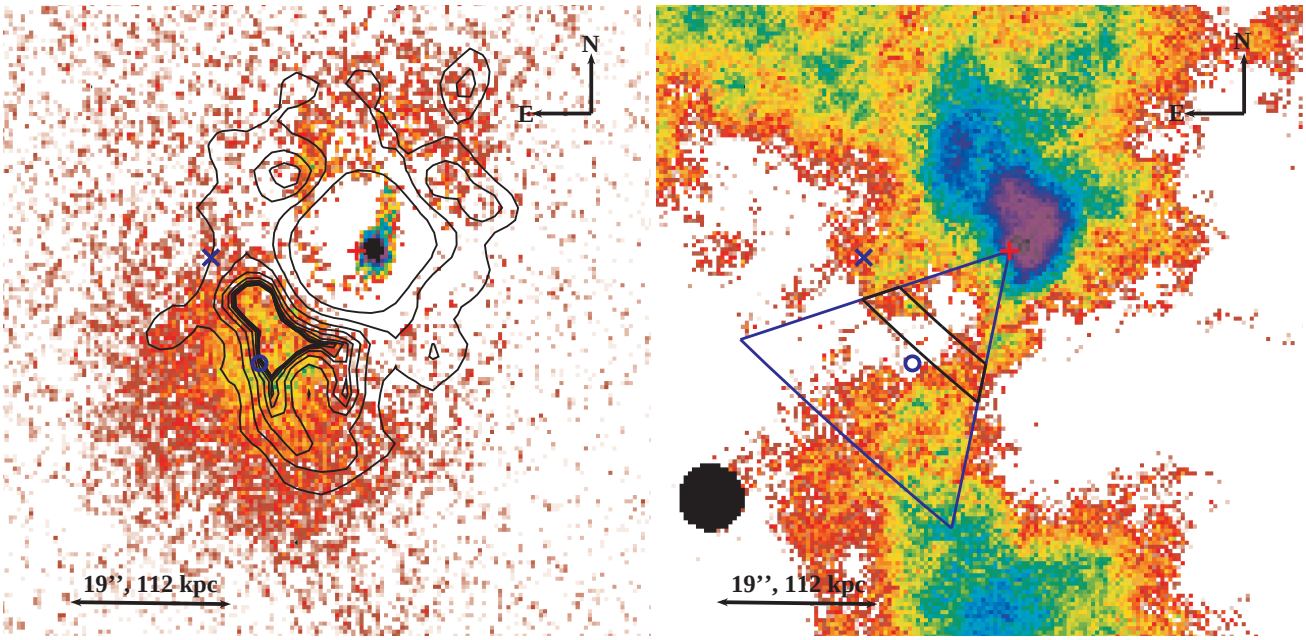


FIG. 11.— (Left) Residuals in log scale with SZ contours overlaid, indicating the maximum SZ decrement over the western shock. (Right) Projected temperature map in linear scale with the elliptical profile covering the western shock front. High gas temperatures coincide with the western and eastern shocks, while lower gas temperature are found in the subcluster core and tail. The region enclosed in black corresponds to the gas build up at the shock front seen in the surface brightness profile, shown in Figure 12.

ure 12 for the profile with shock region in red, and right panel of Figure 11 for the profile's location and shock region enclosed in black. High temperatures, high surface brightness, and a significant SZ decrement in this region suggest that the edge is the western shock front of the subcluster's Mach cone.

The opening angle $\mu$ of the Mach cone can be calculated by (Markevitch & Vikhlinin 2007)

$$sin(\mu) = \mathcal{M}^{-1}. \quad (19)$$

For our calculated eastern Mach number of $1.25 \pm 0.08$, we predict an opening angle of $\mu = 53.1 \pm 0.1$ degrees. Assuming the Mach cone is defined as the angle between the eastern shock edge (see Table 10) and the SZ decrement, we measure an opening angle $\mu \approx 50$ degrees, in good agreement with the predicted value.

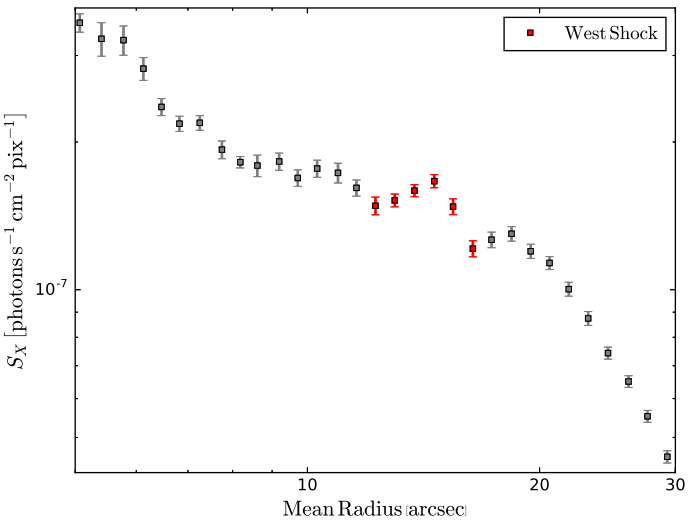


FIG. 12.— Elliptical surface brightness profile centered on the primary cD and aligned with the western shock front. The pile up of gas over the front is highlighted in red. The red points correspond to the region enclosed in black in Figure 11.

## 5. CLUSTER MERGER HISTORY: A COMPARISON TO SIMULATIONS

To constrain the cluster's merger history, it is important to compare our observations with simulations. In Figure 13 we present the same simulation and labels shown in Johnson et al. (2012), who argue that the subcluster is on its second pass around the primary cluster. The simulation initial conditions are described in ZuHone (2011) and employ a mass ratio of the primary cluster to the subcluster of 10 and an impact parameter of $\sim 1$ Mpc. The subcluster is on a clockwise orbit about the primary cluster, such that it first passes the primary

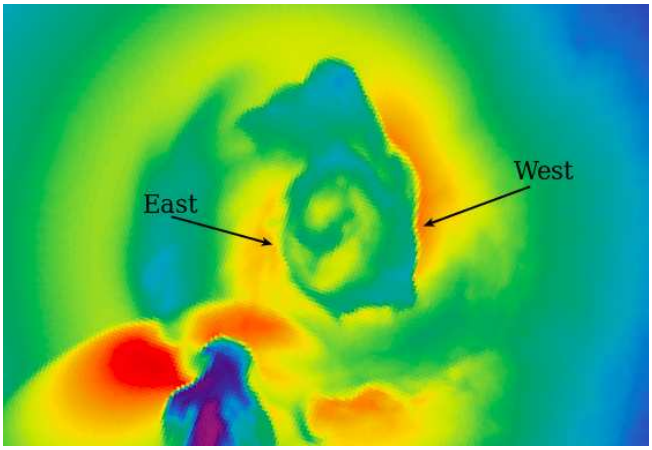


FIG. 13.— A simulated spectroscopic-like projected temperature map from ZuHone (2011) and Johnson et al. (2012). We label the same edges as Johnson et al. (2012).

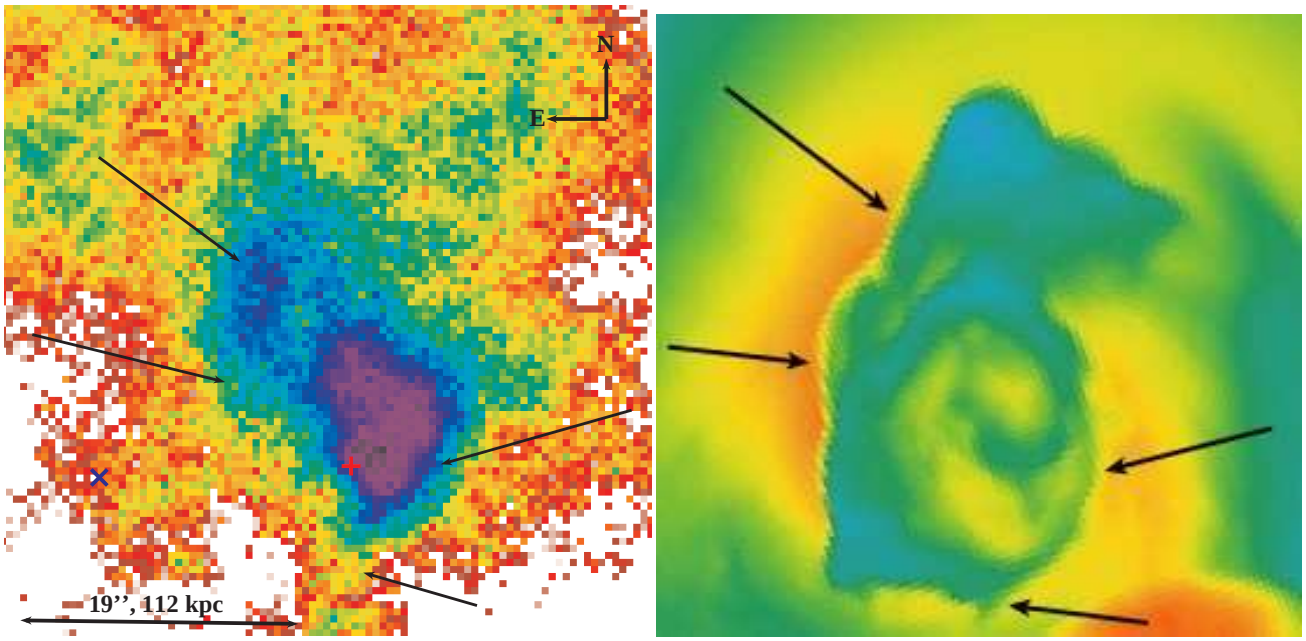


FIG. 14.— In the left panel we show the projected temperature map with cold fronts highlighted. To the right we display the same simulated projected temperature map as in Figure 13 flipped about its N-S axis. We label edges that appear to match those found in the data.

cluster in the west. The simulation captures the subcluster's position and the shock fronts well, in comparison with the X-ray data. However, the cold front locations are not consistent with our observations. In the simulations, the eastern edge is closer to the primary BCG, suggesting that it formed later than the western cold front, but our observations definitively show that the western cold front is closer to the primary BCG. Thus our data suggest that the western cold front formed more recently than the eastern cold front. This leads us to consider the possibility that more than 1 subcluster has perturbed RXJ1347.

In the right panel of Figure 14, we display the same simulation but flipped about the N-S axis such that the subcluster perturber in the simulation is now in a counterclockwise orbit, first passing to the east of the primary cluster. The merger is in the plane of the sky, and we compare our temperature map to this simulation in the left panel. If we ignore the location of the subcluster in the simulation (now in the southwest), we find many similarities between our deep *Chandra* observations and the simulation. The four cold fronts forming a clockwise spiral in the observations can be located in the simulation. We denote these fronts with arrows in both the simulation and the temperature map. The fronts also form a clockwise spiral in the simulation. The fan found in the X-ray observations, and most prominently seen in our residuals image, is similar to the cool gas forming part of the spiral that extends to the north and northwest in the simulation.

As the subcluster passes the primary cluster, it transfers angular momentum (Ascasibar & Markevitch 2006), so we expect the observed clockwise spiral, seen in Figure 1 and confirmed by our cold front analysis, to have been caused by interaction with a subcluster on a counterclockwise orbit around the primary cluster. The clockwise spiral in the flipped simulation supports this scenario. This discrepancy between the observed subcluster to the southeast moving in a clockwise orbit, and the clockwise sloshing spiral in the primary cluster produced in simulations by multiple passes of a perturber moving in a counterclockwise orbit, suggests that the observed subcluster may be on its first pass through the primary cluster, while the clockwise sloshing spiral was caused by earlier encounters with a different subcluster moving in a counterclockwise orbit. In this scenario, the observed subcluster is being ram-pressure stripped while shock heating the cluster gas. The earlier perturber, whose interaction caused the sloshing spiral, may no longer be visible in X-rays because nearly all of its gas has already been stripped. RXJ1347 is in a $\sim 20$ Mpc filament, so it would not be surprising if it had previously interacted with another object in this structure (Verdugo et al. 2012).

We searched the literature for evidence in other wavelengths of a second merging subcluster. Lu et al. (2010) find a massive cluster located $\sim 7$ Mpc southwest of RXJ1347 (RXJ1347-SW) with $\sigma = 780 \pm 100$ km s$^{-1}$, $M_{200} = 3.4^{+1.4}_{-1.1} \times 10^{14} M_{\odot}$, and mean redshift $0.4708 \pm 0.0006$. RXJ1347-SW has a large relative radial velocity of 4000 km s$^{-1}$. Lu et al. (2010) argue the likelihood RXJ1347-SW is falling into RXJ1347 is low. Nonetheless, the concentration of galaxies between RXJ1347 and RXJ1347-SW in velocity space implies the two clusters are physically linked by the same large scale filament.

The recent strong lensing analysis of Köhlinger & Schmidt (2014), using redshift measurements from the Cluster Lensing and Supernova survey (CLASH, Postman et al. 2012), requires two additional perturbers compared to previous lensing analyses (Halkola et al. 2008; Bradač et al. 2008) to model the observed arc geometry. One is a dark halo aligned with a faint $z_{phot} > 0.7$ object and not associated with the primary cluster, and the second is a massive ($\sigma_v \sim 763$ km s$^{-1}$) concentration of cluster galaxies to the NW. While the modeled NW mass component is intriguing as a possible subcluster remnant, it does not appear coincident with any bright cluster galaxy, and no redshift is given. Thus, more work is needed to verify the NW component's existence and association with the primary cluster, as well as to resolve discrepancies be-

tween the CLASH redshift measurements of the lensed systems and those of previous work (Halkola et al. 2008; Bradač et al. 2008).

Another possible scenario is that the orbit of the observed subcluster is not in the plane of the sky and that the observed clockwise orientation of the edges may be due to projection effects. While we consider this latter scenario unlikely, it cannot be ruled out without better simulation studies.

## 6. CONCLUSIONS

With 2.5 times the exposure of previous analyses, we are able to study the gas hydrodynamics of RXJ1347 and its merging subcluster in unprecedented detail. We briefly summarize our key results.

- A series of four cold fronts west, southeast, east, and northeast located at $5\farcs85^{+0.04}_{-0.03}$, $7\farcs10^{+0.07}_{-0.03}$, $11\farcs5^{+1.3}_{-1.2}$, and $16\farcs7^{+0.3}_{-0.5}$ from the primary cluster's cD galaxy, respectively, forms a clockwise spiral, suggesting the merger is in the plane of the sky. The west and east cold fronts correspond to those found by Johnson et al. (2012).

- We measure a subcluster $0.5-2$ keV luminosity of $L_x = 1.3 \times 10^{44}$ erg s$^{-1}$ and infer a lower bound on the total subcluster mass of $3.3 \times 10^{14}$ M$_\odot$.

- We identify the shock from the supersonic infall of the subcluster and measure a density ratio across the shock of $1.38^{+0.16}_{-0.15}$ , corresponding to a Mach number of $1.25 \pm 0.08$ and shock velocity of $2810^{+210}_{-240}$ km s$^{-1}$. The measured opening angle of the Mach cone of $\sim 50$ deg is consistent with this shock interpretation.

- The subcluster's baryonic gas has been stripped from the dark matter peak and leaves a tail behind the subcluster. Asymmetric entropy contours and cooler temperatures extending through the subcluster and tail indicate the subcluster core is being shredded.

- We suggest that the most likely explanation for the observed X-ray features is that the southeast subcluster is on its first passage on a clockwise orbit through the cluster, shock heating the cluster gas as it infalls, while the clockwise sloshing spiral observed in the primary cluster was caused by earlier encounters with a second subcluster moving in a counterclockwise orbit. Better simulations and further observations in other wavelengths are needed to search for remnants of this second perturber and test this scenario.

This work was supported in part by NASA CXC grant GO2-13148X and the Smithsonian Institution. CK gratefully acknowledges support from the Smithsonian Institution Minority Awards Program. This research has made use of data obtained from the Chandra Data Archive and the Chandra Source Catalog, and software provided by the Chandra X-ray Center (CXC) in the application packages CIAO and Sherpa. This work has made use of the NASA/IPAC Extragalactic Database (NED) which is operated by the Jet Propulsion Laboratory, California Institute of Technology, under contract with the National Aeronautics and Space Administration. We would like to thank Maxim Markevitch for helpful discussions and use of his multivariate $\chi^2$ minimization code for fitting the surface brightness profiles, Brian Mason for use of his SZ contours, Jeremy Sanders for help with his GGM filtering technique, Sherry Suyu for useful strong lensing discussions, and the anonymous referee for exceptionally helpful comments.

*Facilities:* CXO (ACIS-I)

REFERENCES


Allen, S. W., Schmidt, R. W., & Fabian, A. C. 2002, MNRAS, 335, 256
Anders, E., & Grevesse, N. 1989, Geochim. Cosmochim. Acta, 53, 197
Ascasibar, Y., & Markevitch, M. 2006, ApJ, 650, 102
Bautz, M. W., et al. 1998, in Society of Photo-Optical Instrumentation Engineers (SPIE) Conference Series, Vol. 3444, X-Ray Optics, Instruments, and Missions, ed. R. B. Hoover & A. B. Walker, 210–224
Bradač, M., et al. 2008, ApJ, 681, 187
Cash, W. 1979, ApJ, 228, 939
Cohen, J. G., & Kneib, J.-P. 2002, ApJ, 573, 524
Evans, I. N., et al. 2010, ApJS, 189, 37
Ferrari, C., et al. 2011, A&A, 534, L12
Finoguenov, A., Sarazin, C. L., Nakazawa, K., Wik, D. R., & Clarke, T. E. 2010, ApJ, 715, 1143
Fruscione, A., et al. 2006, in Society of Photo-Optical Instrumentation Engineers (SPIE) Conference Series, Vol. 6270, Society of Photo-Optical Instrumentation Engineers (SPIE) Conference Series
Fujita, Y., Matsumoto, T., & Wada, K. 2004a, ApJ, 612, L9
Fujita, Y., Sarazin, C. L., Reiprich, T. H., Andernach, H., Ehle, M., Murgia, M., Rudnick, L., & Slee, O. B. 2004b, ApJ, 616, 157
Fujita, Y., Suzuki, T. K., & Wada, K. 2004c, ApJ, 600, 650
Garmire, G. P., et al., eds. 1992, The AXAF CCD imaging spectrometer
Gitti, M., Brunetti, G., & Setti, G. 2002, A&A, 386, 456
Gitti, M., Piffaretti, R., & Schindler, S. 2007, A&A, 472, 383
Gitti, M., & Schindler, S. 2004, A&A, 427, L9
Halkola, A., Hildebrandt, H., Schrabback, T., Lombardi, M., Bradač, M., Erben, T., Schneider, P., & Wuttke, D. 2008, A&A, 481, 65
Johnson, R. E., Zuhone, J., Jones, C., Forman, W. R., & Markevitch, M. 2012, ApJ, 751, 95
Jones, C., & Forman, W. 1984, ApJ, 276, 38
Kitayama, T., Komatsu, E., Ota, N., Kuwabara, T., Suto, Y., Yoshikawa, K., Hattori, M., & Matsuo, H. 2004, PASJ, 56, 17
Köhlinger, F., & Schmidt, R. W. 2014, MNRAS, 437, 1858
Komatsu, E., et al. 2001, PASJ, 53, 57
Korngut, P. M., et al. 2011, ApJ, 734, 10
Lu, T., et al. 2010, MNRAS, 403, 1787
Machacek, M. E., Jerius, D., Kraft, R., Forman, W. R., Jones, C., Randall, S., Giacintucci, S., & Sun, M. 2011, ApJ, 743, 15
Markevitch, M., Gonzalez, A. H., David, L., Vikhlinin, A., Murray, S., Forman, W., Jones, C., & Tucker, W. 2002, ApJ, 567, L27
Markevitch, M., & Vikhlinin, A. 2007, Phys. Rep., 443, 1
Mason, B. S., et al. 2010, ApJ, 716, 739
Mazzotta, P., & Giacintucci, S. 2008, ApJ, 675, L9
Moré, J. J. 1978, The Levenberg-Marquardt algorithm: Implementation and theory, ed. G. A. Watson (Berlin, Heidelberg: Springer Berlin Heidelberg), 105–116
Ota, N., et al. 2008, Astron. Astrophys., 491, 363
Paterno-Mahler, R., Blanton, E. L., Randall, S. W., & Clarke, T. E. 2013, ApJ, 773, 114
Postman, M., et al. 2012, ApJS, 199, 25
Randall, S. W., Jones, C., Markevitch, M., Blanton, E. L., Nulsen, P. E. J., & Forman, W. R. 2009, ApJ, 700, 1404
Roediger, E., Kraft, R. P., Forman, W. R., Nulsen, P. E. J., & Churazov, E. 2013a, ApJ, 764, 60
Roediger, E., Kraft, R. P., Machacek, M. E., Forman, W. R., Nulsen, P. E. J., Jones, C., & Murray, S. S. 2012a, ApJ, 754, 147
Roediger, E., Kraft, R. P., Nulsen, P., Churazov, E., Forman, W., Brüggen, M., & Kokotanekova, R. 2013b, MNRAS, 436, 1721
Roediger, E., Lovisari, L., Dupke, R., Ghizzardi, S., Brüggen, M., Kraft, R. P., & Machacek, M. E. 2012b, MNRAS, 420, 3632
Roediger, E., & Zuhone, J. A. 2012, MNRAS, 419, 1338
Sanders, J. S., Fabian, A. C., Russell, H. R., Walker, S. A., & Blundell, K. M. 2016a, MNRAS, 460, 1898
Sanders, J. S., et al. 2016b, MNRAS, 457, 82
Schindler, S., et al. 1995, A&A, 299, L9
Smith, R. K., Brickhouse, N. S., Liedahl, D. A., & Raymond, J. C. 2001, ApJ, 556, L91
Snowden, S. L., et al. 1997, ApJ, 485, 125
Storn, R., & Price, K. 1995, Differential Evolution - A simple and efficient adaptive scheme for global optimization over continuous spaces
Verdugo, M., Lerchster, M., Böhringer, H., Hildebrandt, H., Ziegler, B. L., Erben, T., Finoguenov, A., & Chon, G. 2012, MNRAS, 421, 1949
Vikhlinin, A., Kravtsov, A., Forman, W., Jones, C., Markevitch, M., Murray, S. S., & Speybroeck, L. V. 2006, The Astrophysical Journal, 640, 691
Vikhlinin, A., et al. 2009a, ApJ, 692, 1033
—. 2009b, ApJ, 692, 1060
Wright, E. L. 2006, PASP, 118, 1711
Zhang, Y.-Y., Andernach, H., Caretta, C. A., Reiprich, T. H., Böhringer, H., Puchwein, E., Sijacki, D., & Girardi, M. 2011, A&A, 526, A105
ZuHone, J. A. 2011, ApJ, 728, 54
ZuHone, J. A., Markevitch, M., Brunetti, G., & Giacintucci, S. 2013, ApJ, 762, 78
ZuHone, J. A., Markevitch, M., & Johnson, R. E. 2010, ApJ, 717, 908
ZuHone, J. A., Markevitch, M., & Lee, D. 2011, ApJ, 743, 16